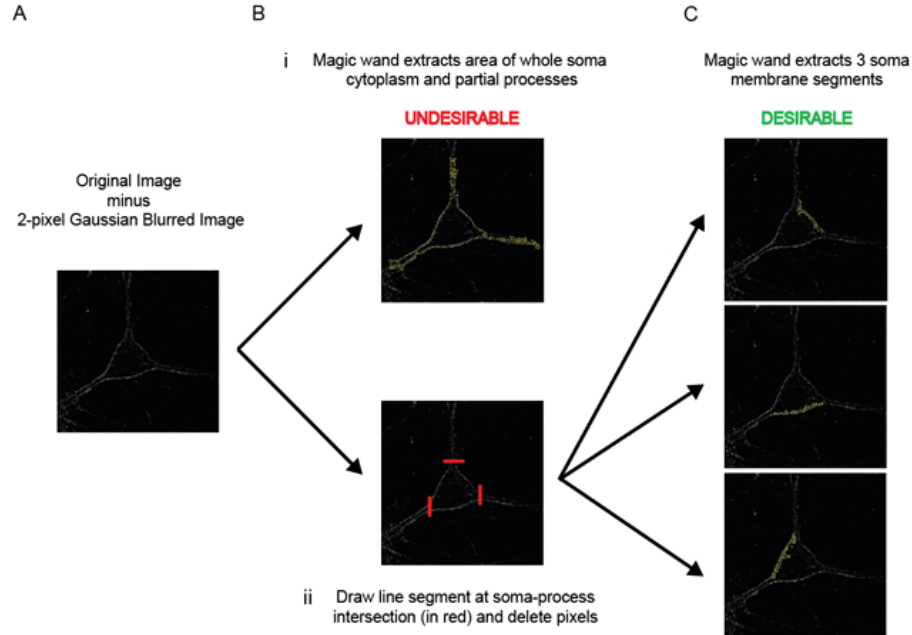
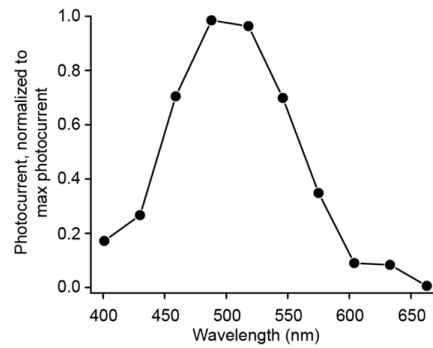


## SUPPLEMENTARY FIGURES AND LEGENDS

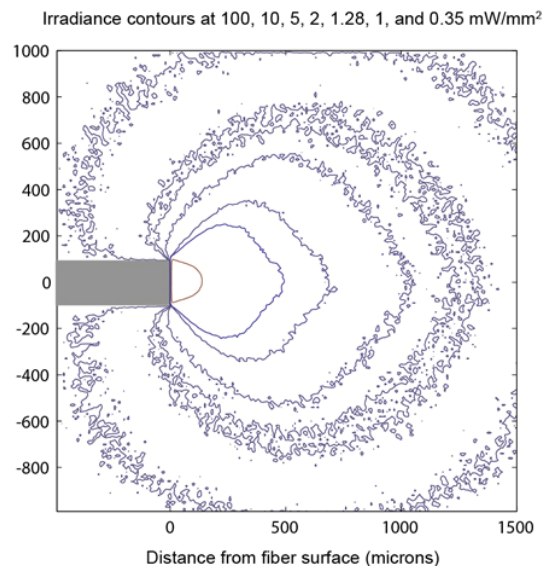


**Supplementary Figure 1.** Outline of the method used for quantitative analysis of opsin-GFP membrane expression in neurons, modified from ref. <sup>1</sup>. **(A)** The cell contour was first enhanced using the blur and subtraction methodology as described in step C of Supplementary Figure S2 of ref. <sup>1</sup>. **(B)** The Magic Wand tool in ImageJ was used to define the pixels corresponding to the cell membrane. **(i)** However, the tool sometimes selected the whole somatic cytoplasm and the processes, because some neuronal processes were too small to be separated into membrane vs. cytosol, causing the appearance of connectedness, and/or because the well-defined membrane processes overlap with other neurons or extend to the edge of the image. **(ii)** Line sections were generated at the apparent boundary of the soma and its processes, to separate sub-resolution image components from the soma (drawn as red here). **(C)** The Magic Wand tool could now select distinct membrane segments of the soma. Membrane expression

was then quantified by taking the area-weighted average of membrane pixel values, in the original image.



**Supplementary Figure 2.** The action spectrum of the *Acetabularium acetabulum* proton pump, measured in HEK 293FT cells (N = 5 cells).



**Supplementary Figure 3.** 593 nm yellow light irradiance in the brain (gray matter) is plotted as a function of location with respect to the tip of an optical fiber (200  $\mu\text{m}$  in

diameter, represented by the gray rectangle shown at left; the irradiance at the surface of the fiber tip was set at 200 mW/mm<sup>2</sup>). Light irradiance was estimated using a Monte Carlo light scattering/absorption simulation. The contours display 100, 10, 5, 2, 1.28, 1, and 0.35 mW/mm<sup>2</sup> irradiances.

## SUPPLEMENTARY NOTES

Using the method of **Supplementary Figure 1**, we found that the absolute expression level of Arch on the plasma membrane was similar to that of Halo ( $p > 0.2$ ,  $N = 5$  cells each). We experimented with adding targeting sequences that improve trafficking, and found that adding a signal sequence from the MHC Class I antigen ('ss')<sup>2</sup> as well as the Kir2.1 ER export sequence ('ER2') (which is part of the sequence that boosts Halo currents by 75%, resulting in eNpHR, ref. <sup>3,4</sup>), did not augment Arch currents ( $p > 0.6$ ,  $N = 16$  Arch cells,  $N = 9$  ss-Arch-ER2 cells). Thus, the effect of a given trafficking-improving sequence on opsin expression is opsin-specific (and perhaps species-specific), but nonetheless deserves further attention. For example, adding the Prolactin signal sequence ('Prl')<sup>5</sup> to the N terminus of Arch trended towards boosting the Arch current (+32%;  $p < 0.08$ ,  $N = 18$  ss-Prl-Arch cells). Improving opsin targeting, however, is unlikely to alter opsin recovery kinetics or light dynamic range.

## SUPPLEMENTARY TABLES

### SUPPLEMENTARY TABLE 1: Molecular screening candidates and references.

Abbreviations	Molecule class	Species of origin	GENBANK Accession	References
---------------	----------------	-------------------	-------------------	------------

---

Halo, NpHR, pHR	halorhodopsin	<i>Natronomas pharaonis</i>	ABQ08589	6-8
sHR, HR	halorhodopsin	<i>Halobacterium salinarum</i>	NP_279315	8,9
aHR-3	archaehalorhodopsin	<i>Halorubrum sodomense</i>	BAA75202	9
aHR-1, SGHR	archaehalorhodopsin	<i>Halorubrum aus-1 (sp. SG1)</i>	CAA49773	9,10
cHR-3	cruxhalorhodopsin	<i>Haloarcula vallismortis</i>	BAA06679	11,12
cHR-5	cruxhalorhodopsin	<i>Haloarcula marismortui</i>	AAV46572	12,13
SquareHOP	square halorhodopsin	<i>Haloquadratum walysbyi</i>	CAJ53165	14
dHR-1	deltahalorhodopsin	<i>Haloterrigena sp. Arg-4</i>	BAA75201	9,12
SalHO, SRU_2780	bacterial halorhodopsin	<i>Salinibacter ruber</i>	AAT76430	15,16
pop	fungal opsin related protein	<i>Podospora anserina (DSM980)</i>	XP_001904282	17
nop-1	fungal opsin related protein	<i>Neospora crassa</i>	XP_959421	18
Mac, LR, Ops	Fungal opsin related protein, bacteriorhodopsin	<i>Leptosphaeria maculans</i>	AAG01180	19
Arch, aR-3	archaerhodopsin	<i>Halorubrum</i>	BAA09452	9

---

		<i>sodomense</i>		
BR	Bacteriorhodopsin	<i>Halobacterium salinarum</i>	CAA23744	9
cR-1	Cruxrhodopsin	<i>Haloarcula argentinensis</i> (sp. <i>arg-1</i> )	BAA06678	20
gPR, BAC31A8	Proteorhodopsin	$\gamma$ - <i>proteobacterium</i> BAC31A8	AAG10475	21,22
bPR, Hot75m4	proteorhodopsin	$\gamma$ - <i>proteobacterium</i> Hot75m4	Q9AFF7	21,22
Ace, AR	Algal bacteriorhodopsin	<i>Acetabularia acetabulum</i>	AAY82897	23

Summary of molecules screened, including abbreviations, molecule classification, species of origin, GenBank accession number, and references. Major molecule types are defined as “bacteriorhodopsins” or “rhodopsins” for outwardly rectifying proton pumps and “halorhodopsins” for inwardly rectifying chloride pumps. Sub-classifications of molecule type are determined by kingdom and/or genus of species of origin (e.g. archaerhodopsin = proton pump from halorubrum genus of halobacteria / haloarchaea).

## SUPPLEMENTARY TABLE 2: Action spectra of screened candidates.

Abbreviations	Molecule class	Species of origin	GENBANK Accession	Primary Peak $\pm$ FWHM (nm), second order Gaussian fit	Spectral Screen Normalization Factor, relative to Halo (see Experimental Procedures)
Halo, NpHR, pHR	halorhodopsin	<i>Natronomas pharaonis</i>	ABQ08589	586 $\pm$ 52	1
sHR, HR	halorhodopsin	<i>Halobacterium salinarum</i>	NP_279315	No measured photocurrent	N/A

aHR-3	archaealrhodopsin	<i>Halorubrum sodomense</i>	BAA75202	586 ± 63	1.18
aHR-1, SGHR	archaealrhodopsin	<i>Halorubrum aus-1 (sp. SG1)</i>	CAA49773	No measured photocurrent	N/A
cHR-3	cruxhalorhodopsin	<i>Haloarcula vallismortis</i>	BAA06679	592 ± 58	1.17
cHR-5	cruxhalorhodopsin	<i>Haloarcula marismortui</i>	AAV46572	594 ± 52	1.10
SquareHOP	square halorhodopsin	<i>Haloquadratum walysbyi</i>	CAJ53165	<sup>1443271919</sup> No measured photocurrent	N/A
dHR-1	deltahalorhodopsin	<i>Haloterrigena sp. Arg-4</i>	BAA75201	No measured photocurrent	N/A
SalHO, SRU_2780 Pop	bacterial halorhodopsin	<i>Salinibacter ruber</i>	AAT76430	582 ± 71	1.12
	fungal opsin related protein	<i>Podospora anserina (DSM980)</i>	XP_001904282	No measured photocurrent	N/A
nop-1	fungal opsin related protein	<i>Neospora crassa</i>	XP_959421	No measured photocurrent	N/A
Mac, LR, Ops	fungal opsin related protein, bacteriorhodopsin	<i>Leptosphaeria maculans</i>	AAG01180	550 ± 69	0.94
Arch, aR-3	archaerhodopsin	<i>Halorubrum sodomense</i>	BAA09452	566 ± 66	1.08
BR	bacteriorhodopsin	<i>Halobacterium salinarum</i>	CAA23744	572 ± 75	1.26
cR-1	cruxrhodopsin	<i>Haloarcula argentinensis</i>	BAA06678	557 ± 67	1.23
gPR, BAC31A8	proteorhodopsin	$\gamma$ - <i>proteobacterium BAC31A8</i>	AAG10475	No measured photocurrent	N/A
bPR, Hot75m4	proteorhodopsin	$\gamma$ - <i>proteobacterium Hot75m4</i>	Q9AFF7	No measured photocurrent	N/A
Ace, AR	algal bacteriorhodopsin	<i>Acetabularia acetabulum</i>	AAY82897	505 ± 57	0.98

Reported peaks and full-width at half-maximum values are from second order Gaussian fits, in order to account for the characteristic “shoulder” of rhodopsins. “Spectral Screen Normalization Factor” accounts for differences in measured photocurrents due to varying excitation efficiencies via use of limited bandpass illumination filters (575 ± 25 nm, 535 ± 25 nm) for all molecules in the screen (see **Supplementary Methods** for normalization protocol). All data reported was measured in neurons, except for Ace (*Acetabularia acetabulum* bacteriorhodopsin homolog), which was measured in HEK 293FT cells (**Supplementary Figure 2**), in order to obtain a precise spectrum given the very low currents observed in neurons.

**SUPPLEMENTARY TABLE 3: Action spectrum and spontaneous recovery to active pumping state in the dark for *N. pharaonis* halorhodopsin (Halo, NpHR) point mutants examined in HEK293FT cells.**

<b>Halo point mutant</b>	<b>Homologous <i>H. salinarum</i> HR residue</b>	<b>Homologous <i>H. salinarum</i> BR residue</b>	<b>Primary predicted outcome of mutation</b>	<b>Primary Peak <math>\pm</math> FWHM (nm), second order Gaussian fit</b>	<b>Recovery of active pumping in dark?</b>
Wild type	N/A	N/A	N/A	584 $\pm$ 51	No
T126H	T111	D85	Recovery	No measured photocurrent	No
T126R	T111	D85	Recovery	No measured photocurrent	No
W127F	W112	W86	Spectral shift	No measured photocurrent	No
S130T	S130	T89	Recovery	568 $\pm$ 55	No
S130D	S130	T89	Recovery	No measured photocurrent	No
S130H	S130	T89	Recovery	No measured photocurrent	No
S130R	S130	T89	Recovery	No measured photocurrent	No
A137T	A122	D96	Recovery	585 $\pm$ 52	No
A137D	A122	D96	Recovery	575 $\pm$ 53	No
A137H	A122	D96	Recovery	No measured photocurrent	No
A137R	A122	D96	Recovery	No measured photocurrent	No
G163C	G148	G122	Spectral shift	No measured photocurrent	No
W179F	W164	W137	Spectral shift	No measured photocurrent	No
S183C	F168	S141	Spectral shift	No measured photocurrent	No
F187M	F172	M145	Spectral shift	589 $\pm$ 52	No
F187A	F172	M145	Spectral shift	No measured photocurrent	No
K215H	R200	R149	Recovery	586 $\pm$ 50	No
K215R	R200	R149	Recovery	575 $\pm$ 51	No
K215Q	R200	R149	Recovery	585 $\pm$ 56	No
T218S	T203	T178	Recovery	582 $\pm$ 53	No
T218D	T203	T178	Recovery	No measured photocurrent	No
T218H	T203	T178	Recovery	No measured photocurrent	No
T218R	T203	T178	Recovery	No measured photocurrent	No
W222F	W207	W182	Spectral shift	No measured photocurrent	No
P226V	P211	P186	Spectral shift	No measured	No

P226G	P211	P186	Spectral shift	photocurrent No measured photocurrent	No
W229F	W214	W189	Spectral shift	587 ± 53	No

Reported peaks and full-width at half-maximum values are from second order Gaussian fits, in order to account for the characteristic “shoulder” of rhodopsins. The column “Primary predicted outcome of mutation” lists hypothesized outcomes as to what parameters of molecular performance might be expected to change, for each mutation. The term “Recovery” refers to spontaneous recovery of the active pumping state in the dark over a timescale of seconds, which holds for Arch and ChR2 but not for Halo (i.e. see **Figure 1D-E** in main text and also ref. <sup>24</sup>). “Recovery” candidate residues were targeted based on their hypothesized roles in chloride affinities and/or transport kinetics, as determined by structure-function studies and mutation studies using other halorhodopsins<sup>25-28</sup>. Spectral residues were targeted based on their predicted retinal flanking locations based on crystal structures, and/or have been shown previously to govern the spectrum of bacteriorhodopsin<sup>29-34</sup>. Alignments to *H. salinarum* halorhodopsin and bacteriorhodopsins were made using NCBI Blast.

## SUPPLEMENTARY METHODS

### Novel opsin reagents: plasmid construction and lentivirus production.

The opsins examined in this study are listed in **Supplementary Table 1**, which describes their molecule classes, species of origin, GenBank Accession numbers, and relevant references. Molecule classes chiefly include bacteriorhodopsins (proton pumps) and halorhodopsins (chloride pumps). Further sub-classifications of ion pump type denote the origin of the species: for example, a “cruxhalorhodopsin” is a chloride pump from the *haloarcu* genus of halobacteria.

Opsins were mammalian codon-optimized, and were synthesized by Genscript (Genscript Corp., NJ). Opsins were fused in frame, without stop codons, ahead of GFP (using BamHI and AgeI) in a lentiviral vector containing the CaMKII promoter<sup>35</sup>, enabling direct neuron transfection, HEK cell transfection (expression in HEK cells is enabled by a ubiquitous promoter upstream of the lentiviral cassette), and lentivirus production (except for *Halobacterium salinarum* halorhodopsin, which was fused to GFP in the vector pEGFP-N3 (using EcoRI and BamHI) and only tested by transfection). eNpHR was synthesized as described before<sup>4</sup>, by inserting the signaling sequence from the acetylcholine receptor beta subunit (amino acid sequence: MRGTPLLLLVVSFLSLLQD; DNA sequence: atgaggggtacgcccctgctcctcgtcgtctctctgttctctctgcttcaggac) at the N-terminus, and the ER2 sequence (amino acid sequence: FCYENEV; DNA sequence: ttctgctacgagaatgaagtg) at the C-terminus of Halo<sup>36,37</sup>. The 'ss' signal sequence from truncated MHC class I antigen corresponded to amino acid sequence (M)VPCTLLLLLAAALAPTQTRA, DNA sequence GTCCCGTGACGCTGCTCCTGCTGTTGGCAGCCGCCCTGGCTCCGACTCAGACGCGGGC C<sup>2</sup>. The 'Pri' Prolactin signal sequence corresponded to amino acid sequence MDSKGSSQKGSRLLLLLVVSNNLLLCQVVS, DNA sequence gacagcaaagggtcgtcgcagaaagggtcccgcctgctcctgctgctggtggtgcaaatctactcttgccagggtggttccacc cccgtc<sup>5,38</sup>. Halo point mutants for HEK cell testing were generated using the QuikChange kit (Stratagene) on the Halo-GFP fusion gene inserted between BamHI and EcoRI sites in the pcDNA 3.1 backbone (Invitrogen). All constructs were verified by sequencing, and codon-optimized sequences of key opsins were submitted to Genbank (mammalian codon-optimized Arch, GU045593; mammalian codon-optimized Arch fused to GFP, GU045594; mammalian codon-optimized Mac, GU045595; mammalian codon-optimized Mac fused to GFP, GU045596;

ss-Prl-Arch, GU045597; ss-Arch-GFP-ER2, GU045598; ss-Prl-Arch-GFP, GU045599) and made available for request at:

<http://syntheticneurobiology.org/protocols>

The amino acid sequence of Arch is:

MDPIALQAGYDLLGDGRPETLWLGIGTLLMLIGTFYFLVRGWGVTDKDAREYYAVTILVPGIASA  
AYLSMFFGIGLTEVTVGEMLDIYYARYADWLFTTPLLDDLALLAKVDRVTIGTLVGVDALMIVT  
GLIGALSHTAIARYSWWLFSTICMIVVLYFLATSLRSAAKERGPEVASTFNTLTALVVLWTAYPI  
LWIIGTEGAGVVGLGIETLLFMVLDVTAKVGFILLRSRAILGDTEAPEPSAGADVSAAD.

The amino acid sequence for Mac is:

MIVDQFEEVLMKTSQLFPLPTATQSAQPTHVAPVPTVLPDTPITYETVGDSGSKTLWVVFVLMMLIA  
SAAFTALSWKIPVNRRLYHVITTIITLTAALSYFAMATGHGVALNKIVIRTQHDHVPDITYETVYRQ  
VYYARYIDWAITTPLLLLDLGLLAGMSGAHIFMAIVADLIMVLTGLFAAFGSEGTPQKWGWYTIA  
CIAYIFVWHLVNLGGANARVKGEKLSFFVAIGAYTLILWTAYPIVWGLADGARKIGVDGEIAY  
AVLDVLAKGVFGAWLLVTHANLRESDELNGFWANGLNREGAIRIGEDDGA.

Replication-incompetent VSVg-pseudotyped lentivirus was produced as previously described<sup>39</sup>, which allows the preparation of clean, non-toxic, high-titer virus (roughly estimated at  $\sim 10^9$ - $10^{10}$  infectious units/mL). Briefly, HEK293FT cells (Invitrogen) were transfected with the lentiviral plasmid, the viral helper plasmid p $\Delta$ 8.74, and the pseudotyping plasmid pMD2.G. The supernatant of transfected HEK cells containing virus was then collected 48 hours after

transfection, purified, and then pelleted through ultracentrifugation. Lentivirus pellet was resuspended in phosphate buffered saline (PBS) and stored at  $-80^{\circ}\text{C}$  until further usage *in vitro* or *in vivo*.

### **Hippocampal and cortical neuron culture preparation, transfection, infection, and imaging.**

All procedures involving animals were in accordance with the National Institutes of Health Guide for the care and use of laboratory animals and approved by the Massachusetts Institute of Technology Animal Care and Use Committee. Swiss Webster or C57 mice (Taconic or Jackson Labs) were used. For hippocampal cultures, hippocampal regions of postnatal day 0 or day 1 mice were isolated and digested with trypsin (1 mg/ml) for  $\sim 12$  min, and then treated with Hanks solution supplemented with 10-20% fetal bovine serum and trypsin inhibitor (Sigma). Tissue was then mechanically dissociated with Pasteur pipettes, and centrifuged at 1000 rpm at  $4^{\circ}\text{C}$  for 10 min. Dissociated neurons were plated at a density of approximately four hippocampi per 20 glass coverslips, coated with Matrigel (BD Biosciences). For cortical cultures, dissociated mouse cortical neurons (postnatal day 0 or 1) were prepared as previously described<sup>40</sup>, and plated at a density of 100-200k per glass coverslip coated with Matrigel (BD Biosciences). Cultures were maintained in Neurobasal Medium supplemented with B27 (Invitrogen) and glutamine. Hippocampal and cortical cultures were used interchangeably; no differences in reagent performance were noted.

Neurons were transfected at 3-5 days *in vitro* using calcium phosphate (Invitrogen). GFP fluorescence was used to identify successfully transfected neurons. Alternatively, neurons were infected with 0.1-1  $\mu\text{l}$  of lentivirus per well at 3-5 days *in vitro*. Throughout the paper, neurons

were transfected unless indicated as having been infected. All images and electrophysiological recordings were made on neurons 9–14 days *in vitro* (approximately 6–10 days after transfection or viral infection).

Confocal images of infected neurons in culture (briefly fixed in 4% paraformaldehyde) were obtained with a Zeiss LSM 510 confocal microscope (63X magnification objective lens). Culture images were maximum intensity projections made from sets of 5 images (1.0  $\mu\text{m}$  image plane thickness) spaced along the z-axis by 0.5 micron steps. Quantitative confocal analysis of membrane expression of opsins was performed using infected neurons in culture (10 days post-infection, briefly fixed in 4% paraformaldehyde). Images were obtained with a Zeiss LSM 510 confocal microscope (63X magnification objective lens), always with the same illumination and observation parameters to avoid procedural variability. Given the near-100% viral infection rate, isolated neurons were chosen for analysis in order to reduce background fluorescence from nearby neurons and their processes. Images were analyzed in ImageJ (National Institutes of Health), based on a neuron-adapted version of a previously reported algorithm<sup>1</sup> used to assay membrane expression of channelrhodopsins and channelrhodopsin variants in HEK cells. An image was first filtered with a 2-pixel Gaussian blur, and the filtered image was subtracted from the original one to enhance the contour of the cell. (These steps are exactly the same as those utilized before in HEK cells<sup>1</sup>; an example of the mathematically enhanced contour is shown in **Supplementary Figure 1A**.) However, because the membranes of neurons do not form simple shapes like the HEK cells as the original algorithm was designed for (**Supplementary Figure 1Bi**), we applied black line sections to separate the neuronal cell body from the processes, as demonstrated in **Supplementary Figure 1Bii** (where the line is in red to aid the eye for these pictures). The magic wand can then accurately select the somatic membrane segments of a neuron (see **Supplementary Figure 1C**), which can then be analyzed by the pixel intensity-

value extraction method described for HEK cells in ref. <sup>1</sup>. The value of the membrane fluorescence for a given neuron, reported in the text, was then defined as the area-weighted average of the line segments. While this method cannot prove that a given patch of membrane-proximal fluorescence exists exclusively on the outermost membrane (in principle a patch of fluorescence could reside just under the membrane), it does serve to discriminate between surface expression and ER retention, and has previously been validated in predicting functional physiological surface expression<sup>1</sup>.

### ***In vitro* patch clamp recording and optical methods.**

Whole cell patch clamp recordings were made on neurons at 9-14 days *in vitro*, using a Multiclamp 700B amplifier, Digidata 1440 digitizer, and a PC running pClamp (Molecular Devices). During recording, neurons were bathed in Tyrode solution containing (in mM): 125 NaCl, 2 KCl, 3 CaCl<sub>2</sub>, 1 MgCl<sub>2</sub>, 10 HEPES, 30 glucose, 0.01 NBQX, and 0.01 gabazine, at pH 7.3 (NaOH adjusted), and with 305-310 mOsm (sucrose adjusted). Borosilicate glass (Warner) pipettes were filled with a solution containing (in mM): 125 K-Gluconate, 8 NaCl, 0.1 CaCl<sub>2</sub>, 0.6 MgCl<sub>2</sub>, 1 EGTA, 10 HEPES, 4 Mg-ATP, 0.4 Na-GTP, at pH 7.3 (KOH adjusted), and with 295-300 mOsm (sucrose adjusted). Pipette resistance was 5-10 MΩ; access resistance was 10–30 MΩ, monitored throughout the voltage-clamp recording; resting membrane potential was ~ -60 mV in current-clamp recording.

For ion selectivity tests (**Fig. 2A**), neurons were bathed in chloride-free recording solution containing (in mM): 125 Na-Gluconate, 2 K-Gluconate, 3 CaSO<sub>4</sub>, 1 MgSO<sub>4</sub>, 10 HEPES, 30 glucose, 0.01 NBQX, 0.01 gabazine, at pH 7.3 (NaOH adjusted), and with 305-310 mOsm (sucrose adjusted), or potassium-free recording solution containing (in mM): 125 NaCl, 2 CsCl,

3 CaCl<sub>2</sub>, 1 MgCl<sub>2</sub>, 10 HEPES, 30 glucose, 0.01 NBQX, 0.01 gabazine, at pH 7.3 (NaOH adjusted), 305-310 mOsm (sucrose adjusted). During these ion selectivity tests, pipettes were filled with chloride-free pipette solution containing (in mM): 125 K-Gluconate, 8 Na-Gluconate, 0.1 CaSO<sub>4</sub>, 0.6 MgSO<sub>4</sub>, 1 EGTA, 10 HEPES, 4 Mg-ATP, 0.4 Na-GTP, pH 7.3 (KOH adjusted), 295-300 mOsm (sucrose adjusted), or potassium-free pipette solution containing (in mM): 125 Cs-methanesulfonate, 8 Na-Gluconate, 0.1 CaSO<sub>4</sub>, 0.6 MgSO<sub>4</sub>, 1 EGTA, 10 HEPES, 4 Mg-ATP, 0.4 Na-GTP, pH 7.3 (CsOH adjusted), 295-300 mOsm (sucrose adjusted). During resting membrane potential shifting (**Fig. 2B**), neurons were bathed in recording solution containing (in mM): 125 N-methyl-D-glucamine, 2 Cs-methanesulfonate, 3 CdSO<sub>4</sub>, 1 MgSO<sub>4</sub>, 10 HEPES, 30 glucose, 0.01 NBQX, 0.01 gabazine, pH 7.3 (H<sub>2</sub>SO<sub>4</sub> adjusted), 305-310 mOsm (sucrose adjusted), and pipettes were also filled with analogous solutions containing (in mM): 125 Cs-methanesulfonate, 8 N-methyl-D-glucamine, 0.1 CdSO<sub>4</sub>, 0.6 MgSO<sub>4</sub>, 1 EGTA, 10 HEPES, 4 Mg-ATP, 0.4 Tris-GTP, pH 7.3 (CsOH adjusted), 295-300 mOsm (sucrose adjusted).

Photocurrents were measured with 1-second or 15-second duration light pulses in neurons voltage clamped at -60mV. Light-induced membrane hyperpolarizations were measured with 1-second light pulses, in neurons current clamped at their resting membrane potential. For all experiments except for the action spectrum characterization experiments, a DG-4 optical switch with 300 W xenon lamp (Sutter Instruments) was used to deliver light pulses. The DG-4 was controlled via TTL pulses generated through a Digidata signal generator. A 575 ± 25 nm bandpass filter (Chroma) was used to deliver yellow light, and a 535 ± 25 nm filter was used to deliver green light. For selective activation of Halo versus Mac at different wavelengths (**Fig. 4**), a 470 ± 20 nm bandpass filter (Chroma) was used to deliver blue light (0.92 mW/mm<sup>2</sup>, through a 40x objective), and a 630 ± 15 (Chroma) was used to deliver red light (2.6 mW/mm<sup>2</sup>). For action

spectrum characterization (**Fig. 1B**, **Fig. 4A**, **Supplementary Table 2**), a Till Photonics PolyChrome V, 150 W Xenon, 15nm monochromator bandwidth, was used.

Data was analyzed using Clampfit (Molecular Devices) and MATLAB (Mathworks, Inc.). Statistical analysis and curve fitting was done with Statview (SAS Institute), MATLAB, or Origin (OriginLab). Reported action spectra are second-order Gaussian fits (performed in MATLAB), because action spectra were asymmetric, with a broad “shoulder” at wavelengths shorter than the primary peak wavelength.

For the initial screening of photocurrents (**Fig. 1A**), yellow light ( $575 \pm 25$  nm,  $7.8$  mW/mm<sup>2</sup>, through a 40x lens) was chiefly used (see below for exceptions); accordingly, in order to adjust the screen data to reflect the photocurrent for each molecule that would have been observed at its respective spectral maximum, photocurrents were spectrum normalized by calculating the overlap integral between the second-order Gaussian fit of the action spectrum for each molecule and the passband of the yellow illumination filter used for the screen (or in other words, integrating the Gaussian fit between 550 and 600 nm), and then dividing that value by the integral of the whole action spectrum for that molecule. These resultant ratios, or “Spectral Screen Normalization Factors,” are summarized (normalized to that ratio for Halo itself) in the rightmost column of **Supplementary Table 2**. In the cases of gPR, bPR, and the *Leptosphaeria maculans* (Mac, LR, Ops) and *Acetabularia acetabulum* (Ace, AR) proton pump opsins, green light ( $535 \pm 25$  nm,  $9.4$  mW/mm<sup>2</sup>, through a 40x lens) was used during the screen, due to the significantly blue-shifted action spectrum of these genes. These four spectra were also normalized to the respective spectral maxima of each molecule, as described above, as well as weighted by the output power of the lamp. All screen photocurrents and spectra (**Fig.**

**1A, Fig. 1B, Fig. 4A, Supplementary Table 2**) were measured in neurons except for the action spectrum of Ace (**Supplementary Figure 2**), which was recorded in HEK 293FT cells for better resolution (due to the extremely small currents of Ace in neurons, **Fig. 1A**).

In order to extend our power characterization of Arch beyond the power of the yellow light available on our microscope using the configuration that we utilized (7.8 mW/mm<sup>2</sup> irradiance, through a 40x lens), we extrapolated to higher effective yellow powers by equating various powers of unfiltered white light illumination from the DG4, to approximate effective yellow power equivalents (**Fig. 1Fii**). These effective irradiances were estimated by adjusting the output power of unfiltered white light from the DG4, and comparing the photocurrents vs. those generated with 575 ± 25 nm yellow light in the same Arch-expressing neuron, at low light powers, until the photocurrent magnitudes were similar ( $p > 0.7$ , paired t-test; N = 6). In support of this method for estimating effective irradiances, we did not observe noticeable photocycle-accelerating effects of non-yellow light for Arch. Light power-photocurrent curves, thus estimated, were fitted with a Hill plot (**Fig. 1F**). To compare to Arch, Halo currents measured for the dose response experiment (**Fig. 1F**) were obtained using a Halo variant that demonstrated similar photocurrent densities compared to unmodified Halo ( $p > 0.7$ , t-test; N = 16), bearing a N-terminal signal sequence from a truncated MHC class I antigen (VPCTLLLLLAAALAPTQTRA, see above) and the C-terminal golgi export sequence from bovine rhodopsin (TETSQVAPA); these measurements were then scaled by the photocurrent ratio between Halo and this variant measured at 7.8 mW/mm<sup>2</sup>, to yield the curve shown in **Fig. 1F**.

**HEK cell culture, transfection, and electrophysiology.**

HEK 293FT cells (Invitrogen) were maintained in DMEM medium (Cellgro) supplemented with 10% fetal bovine serum (Invitrogen), 1% penicillin/streptomycin (Cellgro) and 1% sodium pyruvate (Biowhittaker). For recording, cells were plated at 5-10% confluence on uncoated glass coverslips, where they adhered to surfaces typically within 12-18 hours. Adherent cells were transfected using TransIT 293 transfection kits (Mirus). Cells were recorded by whole-cell patch clamp 1.5 – 2 days later, as described above for neurons, except that they were voltage clamped at -40 mV, with a Tyrode bath solution lacking GABA<sub>A</sub> and NBQX.

### **Intracellular pH imaging.**

Intracellular pH (denoted pH<sub>i</sub>) imaging was performed using a cell-permeant ratiometric fluorescent dye, carboxy-SNARF-1 AM ester (Invitrogen), based on previously reported methods<sup>41,42</sup>. In order to eliminate background fluorescence that would interfere with pH<sub>i</sub> imaging using SNARF-1, we utilized the fusion protein comprising Arch and cyan fluorescent protein (CFP). The DG-4 was used to deliver light pulses (6.1 mW/mm<sup>2</sup>, through a 20x lens) via a green 535 ± 25 nm bandpass filter (Chroma). Neurons were loaded with 10 μM SNARF-1-AM ester in Tyrode solution for 10 minutes, and then washed twice with Tyrode. Arch-expressing neurons were identified by their CFP fluorescence (Chroma CFP set, λ<sub>excitation</sub> = 436 ± 20 nm, λ<sub>dichroic</sub> = 455 nm, λ<sub>emission</sub> = 480 ± 20 nm). After waiting 1 additional minute, Arch and the SNARF-1 dye were simultaneously excited with 535 ± 25 nm light, and the dye was imaged near the isosbestic point of the dye for 500 ms using a 610 ± 37.5 nm bandpass filter (λ<sub>dichroic</sub> = 565 nm, Chroma) to obtain a baseline SNARF loading level. After waiting another minute for the neuron to recover its initial pH<sub>i</sub>, the neuron and dye were again excited with green light, and the dye was imaged at various time points with 1 second exposure lengths, using a 640 ± 25 nm bandpass filter (λ<sub>dichroic</sub> = 600 nm, Chroma). Arch-negative neighboring neurons in the same

field of view were imaged to provide a basis for comparison, and also to provide baseline pH of the cells as a point of reference, as done in ref. <sup>41</sup>. Immediately after this period, the dye was again imaged near the isobestic point for 500 ms to assess for photo-bleaching or dye leakage; no change was observed ( $p > 0.7$  comparing before vs. after 60 seconds of illumination;  $n = 5$  neurons).

Calibration of the dye was performed by the “high  $K^+$ /nigericin” method<sup>42</sup>, in which cells were immersed in a high  $K^+$  Tyrode-like solution containing (in mM): 125 KCl, 2 NaCl, 3  $CaCl_2$ , 1  $MgCl_2$ , 10 HEPES, 30 glucose, 0.01 NBQX, 0.01 gabazine, 0.001 TTX, pH 5.5 and pH 8.5 initial stock solutions (KOH adjusted), 305-310 mOsm (sucrose adjusted). The calibration curve was taken between pH 6.75 and 8 ( $N = 51 - 110$  neurons per calibration point; calibration curve linear region goodness of fit  $R^2 = 0.999$ , between pH 7.15 – 8.0). Images were processed using ImageJ (National Institutes of Health).

### **Cell health assays.**

Membrane properties were measured on day 11 *in vitro* (**Fig. 2E-2G**) using algorithms built into pClamp10. Cell death (**Fig. 2D**) was assayed at day 18 *in vitro* by incubating cultured neurons for 10 minutes in 0.04% Trypan Blue (Gibco) in Tyrode solution for 10 minutes at room temperature, washing with Tyrode solution, and then immediately counting the percentage of neurons stained. In order to limit variability across cell cultures and cell ages, Arch and wild type control neurons were chosen from the same cell cultures and tested on the same day.

### **Estimations of thresholds for silencing.**

To acquire the data in **Fig. 3A**, whole-cell current-clamped neurons were somatically injected with 5Hz current pulse trains (15 ms pulse duration, 8 sec train duration) at 200, 350, or 500 pA, with or without yellow light (575 nm) illumination at irradiances of 6, 1.28, or 0.35 mW/mm<sup>2</sup> for 3 seconds, beginning 2 seconds into the current pulse train. Neurons that did not spike at all with 200 pA current pulses (15 ms pulse duration) were discarded. For all remaining cells, the probability of spiking in the dark, given a 200 pA/15 ms current input, was  $84.0 \pm 10.5\%$  and  $82.8 \pm 3.5\%$  for Halo- and Arch-expressing neurons, respectively ( $p > 0.9$ ,  $N = 7-8$  neurons each), and the probability of spiking in the dark was  $\sim 100\%$ , given  $\geq 350$  pA current inputs.

### **Virus injection.**

Under isoflurane anesthesia, 1  $\mu$ L lentivirus was injected through a craniotomy made in the mouse skull, into the motor cortex (0.62 mm anterior, 0.5 mm lateral, and 0.5 mm deep, relative to bregma), or the sensory cortex (0.02 mm posterior, 3.2 mm lateral, and 2.2 mm deep, relative to bregma). Virus was injected at a rate of 0.1-0.2  $\mu$ l/min through a cannula connected via polyethylene tubing to a Hamilton syringe, placed in a syringe pump (Harvard Apparatus). The syringe, tubing, and cannula were filled with silicone oil (Sigma). For mice used for *in vivo* recordings, custom-fabricated plastic headplates were affixed to the skull<sup>43</sup>, and the craniotomy was protected with agar and dental acrylic.

### ***In vivo* physiology, optical neuromodulation, and data analysis.**

Recordings were made in the cortex of headfixed awake mice 1-2 months after virus injection, using glass microelectrodes of 5-20 M $\Omega$  impedance filled with PBS, containing silver/silver-chloride wire electrodes. Signals were amplified with a Multiclamp 700B amplifier and digitized

with a Digidata 1440, using pClamp software (Molecular Devices). A 50 mW yellow laser (SDL-593-050T, Shanghai Dream Laser) was coupled to a 200 micron-diameter optical fiber in a fashion as described previously<sup>39,44</sup>. The laser was controlled via TTL pulses generated through Digidata. Laser light power was measured with an 818-SL photodetector (Newport Co.). An optical fiber was attached to the recording glass electrode, with the tip of the fiber ~600  $\mu\text{m}$  laterally away from and ~500  $\mu\text{m}$  above the tip of the electrode (e.g., ~800 microns from the tip), and guided into the brain with a Siskiyou manipulator at a slow rate of ~1.5  $\mu\text{m}/\text{s}$  to minimize deformation of the cortical surface.

Data was analyzed using MATLAB (Mathworks, Inc.). Spikes were detected and sorted offline using Wave\_clus ([http://vis.caltech.edu/~rodri/Wave\\_clus/Wave\\_clus\\_home.htm](http://vis.caltech.edu/~rodri/Wave_clus/Wave_clus_home.htm)). Neurons suppressed during light were identified by performing a paired t-test, for each neuron, between the baseline firing rate during the 5 second period before light onset vs. during the period of 5 second light illumination, across all trials for that neuron, thresholding at the  $p < 0.05$  significance level, as previously described<sup>39</sup>. Instantaneous firing rate histograms were computed by averaging the instantaneous firing rate for each neuron, across all trials, with a histogram time bin of 20 ms duration. To determine the latency between light onset and the neural response, we swept a 20 ms-long sliding window through the electrophysiology data and looked for the earliest 20 ms period that deviated from baseline firing rate, as assessed by performing a paired t-test for the firing rate during each window vs. during the baseline period, across all trials for each neuron. Latency was defined as the time from light onset to the time at which firing rate was significantly different from baseline for the following 120 ms. The time for after-light suppression to recover back to baseline was calculated similarly.

## **Histology.**

Between 2 and 8 weeks after virus injection, mice were perfused through the left cardiac ventricle with ~20 mL 4% paraformaldehyde in PBS (pH 7.3), and then the brain was removed and sectioned into 120-240  $\mu\text{m}$  coronal sections on a vibratome in ice-cold PBS, and stored in PBS. Slices were mounted with Vectashield solution (Vector Labs), and visualized with a Zeiss LSM 510 confocal microscope using 20x and 63x objective lenses.

## **Monte Carlo modeling of light propagation.**

In MATLAB, we performed Monte Carlo simulation of light scattering and absorption in the brain from light emitted from the end of an optical fiber by dividing a cube of gray matter into a 200 x 200 x 200 grid of voxels corresponding to 10  $\mu\text{m}$  x 10  $\mu\text{m}$  x 10  $\mu\text{m}$  in dimension, using previously-published model parameters and algorithms<sup>45-47</sup>. We interpolated data from ref. <sup>45</sup> to obtain a scattering coefficient for yellow (~593 nm) light in brain gray matter of 13  $\text{mm}^{-1}$ , and an absorption coefficient of 0.028  $\text{mm}^{-1}$ . Since we were interested in light propagation close to the optical fiber, before the orientation of photon trajectories is randomized by multiple scattering events, we used an anisotropic scattering model based upon the Henyey-Greenstein phase function, utilizing an anisotropy parameter of 0.89<sup>45,46</sup>. We launched  $5 \times 10^6$  packets of photons in a fiberlike radiation pattern through a model fiber (Optran 0.48 HPCS, Thorlabs) with a numerical aperture of 0.48, and modeled their propagation into the brain based on the algorithm of ref. <sup>47</sup>. In essence, whenever a photon packet entered a voxel, our program would probabilistically calculate the forecasted traveling distance before the next scattering event. If that traveling distance took the photon packet out of the starting voxel, then the packet would be partially absorbed appropriately for the distance it traveled within the starting voxel, and the process would then restart upon entry of the photon packet into the new voxel. If that traveling

distance ended the trip of the photon packet within the starting voxel, then the packet would be absorbed appropriately for the distance it traveled within the starting voxel, and a new direction of packet propagation would be randomly chosen according to the Henyey-Greenstein function. Using this model, we generated **Supplementary Figure 3**, which shows the contours at which the light irradiance falls off to various percentages of the irradiance of light at the surface of the optical fiber, for yellow light. The model generally agrees with previous measurements, done in brain slices<sup>48</sup>.

## SUPPLEMENTARY REFERENCES

- 1 Wang, H. *et al.* Molecular determinants differentiating photocurrent properties of two channelrhodopsins from *Chlamydomonas*. *J Biol Chem* **284**, 5685-5696 (2009).
- 2 Munoz-Jordan, J. L. *et al.* Inhibition of alpha/beta interferon signaling by the NS4B protein of flaviviruses. *J Virol* **79**, 8004-8013 (2005).
- 3 Zhao, S. *et al.* Improved expression of halorhodopsin for light-induced silencing of neuronal activity. *Brain cell biology* **36**, 141-154 (2008).
- 4 Gradinaru, V., Thompson, K. R. & Deisseroth, K. eNpHR: a *Natronomonas* halorhodopsin enhanced for optogenetic applications. *Brain cell biology* **36**, 129-139 (2008).
- 5 Jungnickel, B. & Rapoport, T. A. A posttargeting signal sequence recognition event in the endoplasmic reticulum membrane. *Cell* **82**, 261-270 (1995).
- 6 Han, X. & Boyden, E. S. Multiple-color optical activation, silencing, and desynchronization of neural activity, with single-spike temporal resolution. *PLoS ONE* **2**, e299 (2007).
- 7 Zhang, F. *et al.* Multimodal fast optical interrogation of neural circuitry. *Nature* **446**, 633-639 (2007).
- 8 Váró, G. Analogies between halorhodopsin and bacteriorhodopsin. *Biochimica et Biophysica Acta (BBA) - Bioenergetics* **1460**, 220-229 (2000).
- 9 Mukohata, Y., Ihara, K., Tamura, T. & Sugiyama, Y. Halobacterial rhodopsins. *J Biochem* **125**, 649-657 (1999).
- 10 Soppa, J., Duschl, J. & Oesterhelt, D. Bacteriorhodopsin, haloopsin, and sensory opsin I of the halobacterial isolate *Halobacterium* sp. strain SG1: three new members of a growing family. *J Bacteriol* **175**, 2720-2726 (1993).

- 11 Kitajima, T. *et al.* Novel bacterial rhodopsins from Haloarcula vallismortis. *Biochem Biophys Res Commun* **220**, 341-345 (1996).
- 12 Klare, J. P., Chizhov, I. & Engelhard, M. Microbial rhodopsins: scaffolds for ion pumps, channels, and sensors. *Results Probl Cell Differ* **45**, 73-122 (2008).
- 13 Baliga, N. S. *et al.* Genome sequence of Haloarcula marismortui: a halophilic archaeon from the Dead Sea. *Genome Res* **14**, 2221-2234 (2004).
- 14 Bolhuis, H. *et al.* The genome of the square archaeon Haloquadratum walsbyi : life at the limits of water activity. *BMC Genomics* **7**, 169 (2006).
- 15 Mongodin, E. F. *et al.* The genome of Salinibacter ruber: convergence and gene exchange among hyperhalophilic bacteria and archaea. *Proc Natl Acad Sci U S A* **102**, 18147-18152 (2005).
- 16 Antón, J. *et al.* in *Adaptation to Life in High Salt Concentrations in Archaea, Bacteria and Eukarya* eds N. Gunde-Cimerman, Plemenitas. A, & A. Oren) 257–266. (Kluwer Academic Publishers, 2005).
- 17 Espagne, E. *et al.* The genome sequence of the model ascomycete fungus Podospora anserina. *Genome Biology* **9**, R77 (2008).
- 18 Bieszke, J. A. *et al.* The nop-1 gene of Neurospora crassa encodes a seven transmembrane helix retinal-binding protein homologous to archaeal rhodopsins. *Proc Natl Acad Sci U S A* **96**, 8034-8039 (1999).
- 19 Waschuk, S. A., Bezerra, A. G., Shi, L. & Brown, L. S. Leptosphaeria rhodopsin: Bacteriorhodopsin-like proton pump from a eukaryote. *Proceedings of the National Academy of Sciences of the United States of America* **102**, 6879-6883, doi:10.1073/pnas.0409659102 (2005).
- 20 Tateno, M., Ihara, K. & Mukohata, Y. The novel ion pump rhodopsins from Haloarcula form a family independent from both the bacteriorhodopsin and archaerhodopsin families/tribes. *Arch Biochem Biophys* **315**, 127-132 (1994).
- 21 Beja, O. *et al.* Bacterial rhodopsin: evidence for a new type of phototrophy in the sea. *Science* **289**, 1902-1906 (2000).
- 22 Wang, W. W., Sineshchekov, O. A., Spudich, E. N. & Spudich, J. L. Spectroscopic and photochemical characterization of a deep ocean proteorhodopsin. *J Biol Chem* **278**, 33985-33991 (2003).
- 23 Tsunoda, S. P. *et al.* H<sup>+</sup>-pumping rhodopsin from the marine alga Acetabularia. *Biophys J* **91**, 1471-1479 (2006).
- 24 Han, X. & Boyden, E. S. Multiple-color optical activation, silencing, and desynchronization of neural activity, with single-spike temporal resolution. *PLoS ONE* **2**, e299 (2007).

- 25 Rudiger, M., Haupts, U., Gerwert, K. & Oesterhelt, D. Chemical reconstitution of a chloride pump inactivated by a single point mutation. *Embo J* **14**, 1599-1606 (1995).
- 26 Rudiger, M. & Oesterhelt, D. Specific arginine and threonine residues control anion binding and transport in the light-driven chloride pump halorhodopsin. *Embo J* **16**, 3813-3821 (1997).
- 27 Sato, M. *et al.* Ser-130 of Natronobacterium pharaonis halorhodopsin is important for the chloride binding. *Biophysical Chemistry* **104**, 209-216 (2003).
- 28 Sato, M. *et al.* Roles of Ser130 and Thr126 in chloride binding and photocycle of pharaonis halorhodopsin. *Journal of biochemistry* **134**, 151-158 (2003).
- 29 Kolbe, M., Besir, H., Essen, L. O. & Oesterhelt, D. Structure of the light-driven chloride pump halorhodopsin at 1.8 Å resolution. *Science* **288**, 1390-1396 (2000).
- 30 Mogi, T., Marti, T. & Khorana, H. G. Structure-function studies on bacteriorhodopsin. IX. Substitutions of tryptophan residues affect protein-retinal interactions in bacteriorhodopsin. *J Biol Chem* **264**, 14197-14201 (1989).
- 31 Mogi, T., Stern, L. J., Chao, B. H. & Khorana, H. G. Structure-function studies on bacteriorhodopsin. VIII. Substitutions of the membrane-embedded prolines 50, 91, and 186: the effects are determined by the substituting amino acids. *J Biol Chem* **264**, 14192-14196 (1989).
- 32 Mogi, T., Stern, L. J., Hackett, N. R. & Khorana, H. G. Bacteriorhodopsin mutants containing single tyrosine to phenylalanine substitutions are all active in proton translocation. *Proc Natl Acad Sci U S A* **84**, 5595-5599 (1987).
- 33 Mogi, T., Stern, L. J., Marti, T., Chao, B. H. & Khorana, H. G. Aspartic acid substitutions affect proton translocation by bacteriorhodopsin. *Proc Natl Acad Sci U S A* **85**, 4148-4152 (1988).
- 34 Greenhalgh, D. A., Farrens, D. L., Subramaniam, S. & Khorana, H. G. Hydrophobic amino acids in the retinal-binding pocket of bacteriorhodopsin. *J Biol Chem* **268**, 20305-20311 (1993).
- 35 Han, X. *et al.* Millisecond-Timescale Optical Control of Neural Dynamics in the Nonhuman Primate Brain. *Neuron* **62**, 191-198 (2009).
- 36 Hofherr, A., Fakler, B. & Klocker, N. Selective Golgi export of Kir2.1 controls the stoichiometry of functional Kir2.x channel heteromers. *Journal of cell science* **118**, 1935-1943 (2005).
- 37 Stockklausner, C. & Klocker, N. Surface expression of inward rectifier potassium channels is controlled by selective Golgi export. *J Biol Chem* **278**, 17000-17005 (2003).
- 38 Kim, S. J., Mitra, D., Salerno, J. R. & Hegde, R. S. Signal sequences control gating of the protein translocation channel in a substrate-specific manner. *Developmental cell* **2**, 207-217 (2002).

- 39 Han, X. *et al.* Millisecond-timescale optical control of neural dynamics in the nonhuman primate brain. *Neuron* **62**, 191-198 (2009).
- 40 Lin, Y. *et al.* Activity-dependent regulation of inhibitory synapse development by Npas4. *Nature* **455**, 1198-1204 (2008).
- 41 Lin, J. Y., Lin, M. Z., Steinbach, P. & Tsien, R. Y. Characterization of engineered channelrhodopsin variants with improved properties and kinetics. *Biophys J* **96**, 1803-1814 (2009).
- 42 Bevensee, M. O. & Boron, W. F. in *pH and brain function* eds Kai Kaila & Bruce R. Ransom) Ch. 8, 129-152 (Wiley-Liss, 1998).
- 43 Boyden, E. S. & Raymond, J. L. Active reversal of motor memories reveals rules governing memory encoding. *Neuron* **39**, 1031-1042 (2003).
- 44 Bernstein, J. *et al.* in *Optical Interactions with Tissue and Cells XIX*. (ed Steven L. Jacques; William P. Roach; Robert J. Thomas) 68540H:68541-68511 (Proceedings of the SPIE).
- 45 Yaroslavsky, A. N. *et al.* Optical properties of selected native and coagulated human brain tissues in vitro in the visible and near infrared spectral range. *Physics in medicine and biology* **47**, 2059-2073 (2002).
- 46 Binzoni, T., Leung, T. S., Gandjbakhche, A. H., Rufenacht, D. & Delpy, D. T. The use of the Henyey-Greenstein phase function in Monte Carlo simulations in biomedical optics. *Physics in medicine and biology* **51**, N313-322 (2006).
- 47 Wang, L., Jacques, S. L. & Zheng, L. MCML--Monte Carlo modeling of light transport in multi-layered tissues. *Computer methods and programs in biomedicine* **47**, 131-146 (1995).
- 48 Bernstein, J. G. *et al.* Prosthetic systems for therapeutic optical activation and silencing of genetically-targeted neurons. *Proceedings - Society of Photo-Optical Instrumentation Engineers* **6854**, 68540H (2008).